Heterogeneous and homogeneous combustion of fuel-lean $C_3H_8/O_2/N_2$ mixtures over rhodium at pressures up to 6 bar

John Mantzaras [a,*], Ran Sui [a,b], Chung K. Law [b], Rolf Bombach [c]

[a] *Laboratory for Scientific Computing and Modeling, Paul Scherrer Institute, CH-5232 Villigen PSI, Switzerland*
[b] *Department of Mechanical and Aerospace Engineering, Princeton University, Princeton, NJ 08544, United States*
[c] *Energy System Integration Platform, Paul Scherrer Institute, CH-5232 Villigen PSI, Switzerland*

Abstract

The heterogeneous and homogeneous combustion of $C_3H_8/O_2/N_2$ mixtures over Rh was investigated at pressures 1-6 bar, catalyst surface temperatures 680-1100 K and C_3H_8-to-O_2 equivalence ratios 0.25-0.52. Non-intrusive laser-based measurements were applied in a channel-flow catalytic reactor and involved 1-D Raman spectroscopy of major gas-phase species across the channel boundary layer for assessing the catalytic reactivity and planar laser induced fluorescence (PLIF) of the OH radical for monitoring homogeneous combustion. Simulations were carried out with a 2-D numerical code that included detailed hetero-/homogeneous chemical reaction mechanisms. By comparing the Raman-measured and predicted transverse profiles of the limiting C_3H_8 reactant, the suitability of a detailed surface reaction mechanism was initially evaluated and subsequently a one-step reaction was constructed, which was applicable for the C_3H_8 total oxidation over Rh at pressures 1 to 6 bar. The catalytic reactivity of C_3H_8 over Rh displayed a $\sim p^{0.14}$ pressure dependence, which was substantially lower than a previously reported $\sim p^{0.70}$ dependence over Pt. The weak pressure dependence of the C_3H_8 reactivity on Rh suggested caution when selecting catalysts for high-pressure power systems (recuperative microreactors, small-scale turbines) fueled with C_3H_8 or LPG (liquefied petroleum gas). Comparisons of PLIF-measured and predicted distributions of the OH radical indicated that the employed gas-phase reaction mechanism captured the onset of homogeneous ignition at pressures greater than or equal to 3 bar as well as the ensuing flame shapes. Predicted and measured homogeneous ignition distances agreed within 2.5% at 6 bar. With decreasing pressure, the predictions yielded gradually increasing but still modest underpredictions (up to 11.2% at 3 bar) of the homogeneous ignition distances. The key gas-phase reactions affecting homogeneous combustion at various pressures were finally identified.
© 2020 The Combustion Institute. Published by Elsevier Inc. All rights reserved.

* Corresponding author.
E-mail address: ioannis.mantzaras@psi.ch
(J. Mantzaras).

1. Introduction

The catalytic total oxidation (CTOX) of propane over noble metals is of prime importance for many industrial systems that include natural-gas-fired power plants using hybrid combustion approaches [1] (natural gas contains up to ~4% propane), catalytic microreactors operating with propane or LPG (liquefied petroleum gas, a propane/butane mixture) [2,3] and catalytic converters in LPG-fueled vehicles [4]. Propane has the advantage that it liquefies at room temperature and modest pressures and is readily accessible in compact containers for consumer applications. Some key physicochemical properties of propane are common among high hydrocarbons, such as its larger-than-unity Lewis number (leading to underadiabatic surface temperatures during fuel-lean propane/air catalytic combustion [5]) and the negative temperature coefficient during its gaseous ignition [6].

Pt is more active than Pd [7] and Rh [8] for propane CTOX, such that most related studies focused on Pt [9–11], with suitable global mechanisms at atmospheric pressure reported in [10,12]. Despite the lower reactivity of Rh towards propane CTOX (and methane CTOX [13]), it can be used as promoter or additive in other noble metals. For example, bimetallic Rh-Pt catalysts are used in automotive converters [8,14], while the addition of Rh on Pd improves the long-term stability of Pd [15]. Light-off temperatures during propane CTOX over Rh have been reported in [16,17]. The CTOX as well as the catalytic partial oxidation (CPOX) of propane on Rh was studied at atmospheric pressure in [18] and detailed chemistry models were constructed for propane [19] and iso-octane/propane [20] CPOX over Rh.

Elevated pressures are relevant for power generation and microreactors. While for methane CTOX there are several high-pressure kinetic studies over Pt, Rh and Pd [13,21–25], there are fewer works for propane. A global catalytic scheme for propane CTOX over Pt valid for 1-7 bar was reported in our earlier work [26], while the performance of a propane-fueled Pt-coated microreactor was assessed in [3] at pressures up to 5 bar. High-pressure kinetic studies for propane CTOX and CPOX over Rh have not been elaborated in the past. The CTOX kinetics of hydrocarbons on noble metals exhibit intricate pressure dependencies due to the oxygen surface blocking at sufficiently low temperatures, a process largely controlled by the O_2 partial pressure above the catalyst [13,21,25–27].

The present work undertakes an investigation of the catalytic and gas-phase combustion of fuel-lean $C_3H_8/O_2/N_2$ mixtures over Rh at pressures 1-6 bar, a range of interest for small-scale industrial turbines and recuperative microreactors. Experiments are carried out in an optically accessible channel-flow catalytic reactor and involve Raman measure-
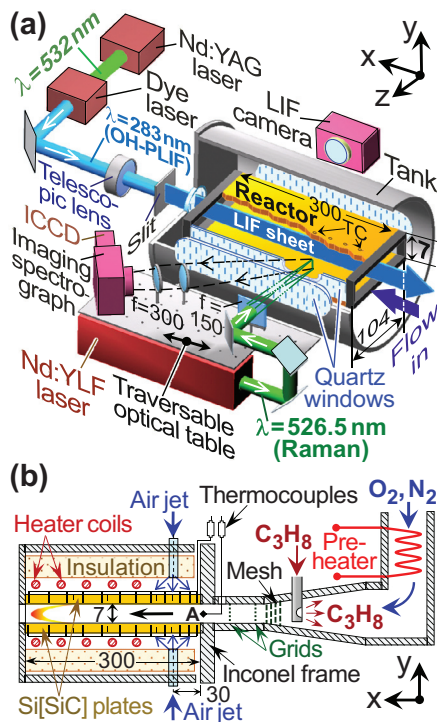

Fig. 1. (a) Test-rig and Raman/OH-PLIF setups, (b) reactor details. Dimensions in mm.

ments of major gas-phase species concentrations for assessing the catalytic reactivity and planar laser induced fluorescence (PLIF) of the OH radical for monitoring homogeneous combustion. Simulations are performed using a 2-D CFD code with detailed hetero-/homogeneous chemistries. Main objectives are to quantify the pressure dependence of the propane catalytic reactivity on Rh and to assess the conditions leading to the onset of homogeneous ignition.

2. Experimental

2.1. High-pressure catalytic reactor

The catalytic channel-flow reactor comprised two horizontal Si[SiC] ceramic plates (300 mm long (-x), 104 mm wide (-z), 9 mm thick, placed 7 mm apart (-y)) and two 3-mm-thick vertical quartz windows (see Fig. 1a and [28]). The inner Si[SiC] surfaces were coated with Rh using plasma vapor deposition. A 1.5-μm-thick non-porous Al_2O_3 layer was first deposited on the Si[SiC] followed by a 2.2-μm-thick Rh layer. This considerably thick Rh layer closely resembled a polycrystalline surface; moreover, X-ray photoelectron spectroscopy (XPS) attested the absence of Al and Si from the catalyst surfaces. Surface temperatures were measured

by S-type thermocouples (12 for each plate, located along the x-y symmetry plane, see Fig. 1), whose beads were affixed 0.9 mm beneath the catalyst by eroding 8.1-mm-deep and 1.2-mm-diameter holes from the uncoated outer Si[SiC] sides. Over the length $100 < x < 300$ mm ($x = 0$ denotes the start of the catalytic plate), two adjustable-power heating coils positioned above/below the two Si[SiC] plates regulated the catalyst temperatures (Fig. 1b). For finer surface temperature control, two adjustable-flow cooling air jets issuing from two rectangular slots (10×100 mm^2 in x-z, located at $x = 30$ mm) impinged on the outer Si[SiC] sides (Fig. 1b).

The reactor was mounted inside an Inconel frame (Fig. 1b) that formed a liner in a high-pressure cylindrical steel tank equipped with two 350-mm-long, 50-mm-high and 35-mm-thick side quartz windows, providing a lateral (-z) optical access (Fig. 1a). Two additional quartz windows at the rear tank flange and the reactor exhaust yielded a streamwise (-x) optical access. Bottles supplied C_3H_8 (99.95%), O_2 and N_2, with three Brooks mass flowmeters regulating the flows. The C_3H_8 bottle was electrically-heated to achieve vapor pressures ~15 bar, which (when considering the flowmeter and supply-line pressure drops) led to reactor pressures up to 6 bar. The mixed O_2/N_2 flows were electrically preheated (Fig. 1b), while C_3H_8 was injected to the preheated O_2/N_2 stream in a 200-mm-long steel conical section (Fig. 1b) that had an ending cross-flow area equal to the channel reactor (104×7 mm^2). A wire mesh and two fine grids (0.5 mm^2 open areas) yielded good mixing of C_3H_8 with O_2/N_2 and uniform exit velocity. At the exit plane of the conical section, hot-wire velocimetry assessed the flow uniformity and NO-PLIF (100 ppmv NO doped into C_3H_8, excitation at 226.25 nm and detection at 240–265 nm) confirmed the good mixing quality: the NO-PLIF images had spatial variations of the intensity less than 2%. A sheathed thermocouple at the conical section end (marked "A" in Fig. 1b) recorded the gas inlet temperature.

2.2. Laser diagnostics

The laser-based techniques are depicted in Fig. 1a and were recently reviewed in [5]. A frequency-doubled pulsed Nd:YLF laser (Quantronix Darwin-Duo, repetition frequency 2 kHz at 526.5 nm, 120 ns pulse duration, 40 mJ pulse energy) provided the Raman excitation. A cylindrical lens ($f = 150$ mm) focused the beam into a ~0.3 mm thick vertical line, which spanned the 7 mm channel height and was offset from the x-y symmetry plane ($z = 15$ mm) to increase the collection angle and minimize thermal beam steering [13,25]. The scattered light was focused by two spherical lenses ($f = 300$ mm) into the entrance slit of a 25 cm spectrograph (Chromex-250i) that had an intensified CCD-camera (Princeton Instru-

ments PI-MAX1024GIII) with 640×255 pixels corresponding to spectral shift and 7-mm channel height, respectively; the 255-pixel-long height was further binned to 64 pixels. A tilted 532 nm holographic notch filter (Kaiser-Optical systems) and an OG550 Schott glass filter suppressed the excitation radiation. Raman measurements were obtained for all major species relevant to CTOX (C_3H_8, O_2, N_2, H_2O and CO_2).

The Nd:YLF laser, the spectrograph and all optics were mounted on a traversable optical table (Fig. 1a), permitting measurements over $8 \leq x \leq 126$ mm. Given the steady operating conditions, Raman-scattered light from ~300,000 laser pulses was integrated on the detector chip to increase the signal-to-noise ratio (SNR). Effective Raman cross-sections, including transmission efficiencies, were evaluated by recording the signals of pressurized C_3H_8, air, N_2-containing mixtures and the true reactive mixtures [26]. Measurement accuracy was ±4% for species concentrations $\geq$ 3% vol. and ±8% for concentrations as low as 0.5% vol., whereas lower compositions could not be accurately resolved. Only N_2 and the excess reactant O_2 never fell (at any location) below the 0.5% vol. detection threshold. Due to low SNR, Raman data points within 0.5-0.7 mm from both walls were discarded (SNR less than 1.5–2.0, depending on beam steering and optical vignetting).

For OH-PLIF, a frequency-doubled pulsed Nd:YAG laser (Quantel YG781C20 CL-D-LNE3, 532 nm, 10 ns pulse duration, 20 Hz repetition rate) pumped a Quantel TDL90-NBP2EWT UVT3 dye laser. The resulting radiation was frequency-doubled at 283.3 nm to excite the A-X(1,0) $Q_1(7)$ OH transition. The excitation beam was transformed by a telescopic lens and a slit-mask into a vertical light sheet propagating counterflow along the x-y symmetry plane (Fig. 1a). An intensified CCD camera (LaVision Imager Compact HiRes-IRO, 1392×1024 pixels) recorded the fluorescence signal at 90° through the reactor and tank side-windows. Fluorescence was collected from the (1-1) and (0-0) transitions at 308 and 314 nm, respectively. Channel areas 100×7 mm^2 (x-y) were recorded on 1360×120 pixels, while the camera was traversed axially to map the full channel length.

3. Numerical

Simulations were performed with a 2-D steady Navier-Stokes CFD code [21]. A staggered orthogonal grid with 480×68 points for the 300×7 mm^2 domain along the x-y symmetry plane yielded grid-independent solutions. Curves fitted through the 12 thermocouple measurements on each plate provided the lower-wall ($y = 0$) and upper-wall ($y = 7$ mm) temperature profiles, which were imposed as energy boundary conditions. The axial ve-

Table 1
Experimental conditions.[a]

Case	p	φ	U_{IN}	T_{IN}	C_3H_8	O_2
1	1.0	0.248	3.94	369	2.56	52.40
2	2.0	0.265	1.64	356	2.81	52.48
3	3.0	0.248	1.24	347	2.56	52.40
4	4.0	0.265	0.78	339	2.81	52.48
5	5.0	0.265	0.62	339	2.81	52.48
6	6.0	0.248	0.60	335	2.56	52.40
7	3.0	0.524	0.49	390	2.97	27.92
8	3.5	0.502	0.42	389	2.75	27.98
9	4.0	0.500	0.35	374	2.75	27.98
10	5.0	0.475	0.28	377	2.76	28.05
11	6.0	0.375	0.23	365	2.07	28.34

[a] Pressure (bar), equivalence ratio, inlet velocity (m/s), inlet temperature (K), inlet C_3H_8 and O_2 (% vol., balance N_2).

locity, temperature, and species mass fractions at the inlet ($x = 0$) were uniform.

For the catalytic oxidation of C_3H_8 on Rh, the detailed mechanism from Karakaya et al. [19,20] was used (17 surface and 7 gaseous species). Although this mechanism was originally developed for CPOX and steam reforming, it provided a starting point for the simulations. Additional simulations were performed with a herein-developed global catalytic step. For propane gas-phase chemistry, the latest San Diego mechanism was used [29] (58 species, 268 reactions) along with its thermodynamic and transport databases. Surface and gas-phase chemical reaction rates were evaluated with Chemkin [30,31] and a mixture-average species transport model was used [32].

4. Results and discussion

Pressures 1-6 bar and fuel-lean C_3H_8/O_2 equivalence ratios $\varphi = 0.248$-0.524 were investigated (Table 1). The small differences in φ for Cases 1–6 were due to the long combustion stabilization times (> 1 hr) that did not allow for precise fine-tuning of these parameters; nonetheless, these differences were fully accounted for in the simulations and hence did not affect the deduced physics. The catalytic reactivity was assessed with Raman measurements in Cases 1-6, while homogeneous combustion was studied with OH-PLIF in Cases 7-11. The heat release rate did not vary significantly, since in most cases the volumetric content of the deficient C_3H_8 reactant varied modestly over the range 2.56-2.97%. However, the O_2 content in Cases 1-6 was nearly twice as high as that in Cases 7-11, to facilitate Raman measurements of this reactive species. In the catalytic reactivity studies of Cases 1-6, OH-PLIF was still applied to ensure the absence of homogeneous combustion. This was a key requirement as it negated potential falsification of the catalytic kinetics by gaseous kinetics [5]. The OH-PLIF Cases 7-11 had somewhat higher inlet temperatures (Table 1) and longer residence times

(lower U_{IN}) to facilitate homogeneous ignition. All flows were laminar with inlet Reynolds numbers 430-1280 based on the channel height.

4.1. Assessment of catalytic reactivity

Raman-measured and predicted (with the catalytic mechanism from Karakaya et al. [19]) transverse profiles of the deficient reactant C_3H_8 and the product H_2O are presented in Figs. 2 and 3 at five axial positions, while the corresponding wall temperature profiles are shown in Fig. 4. For clarity, up to 18 of the 64 Raman data points are plotted over the experimentally-resolvable length $0.6 \lesssim y \lesssim 6.4$ mm. Homogeneous combustion was absent in Cases 1-6 (attested by both OH-PLIF and simulations), such that the profiles in Figs. 2-3 were solely determined by catalytic chemistry. Transport-limited (infinitely-fast catalytic chemistry) simulations for the last axial position $x = 126$ mm are also included in Figs. 2–3, marked as TRL. The TRL profiles demarcated physical lower (upper) bounds for the C_3H_8 (H_2O) mole fractions and the measurements clearly obeyed these bounds. All cases fell in the kinetically-controlled regime, comfortably away from the transport limit (i.e. the mole fractions of the deficient reactant C_3H_8 in Figs. 2–3 were well-above zero at both walls), which was a cardinal prerequisite for assessing the catalytic reactivity [5]. Wall temperatures 680-970 K were attained over the extent of the Raman measurements (Fig. 4) with the lower walls being typically hotter, thus yielding modestly asymmetric profiles in Figs. 2–3.

Simulations at 1 bar in Fig. 2(1a) captured very well the measured C_3H_8 mole fraction profiles. At 2 bar (Fig. 2(2a)) the good agreement was still maintained although the catalytic reactivity was modestly overpredicted, as illustrated at the last two axial positions by the slightly lower computed near-wall C_3H_8 mole fractions compared to the measurements (stars and diamonds symbols). The catalytic reactivity overprediction progressively intensified with rising pressures (Figs. 3(3a-6a)). For
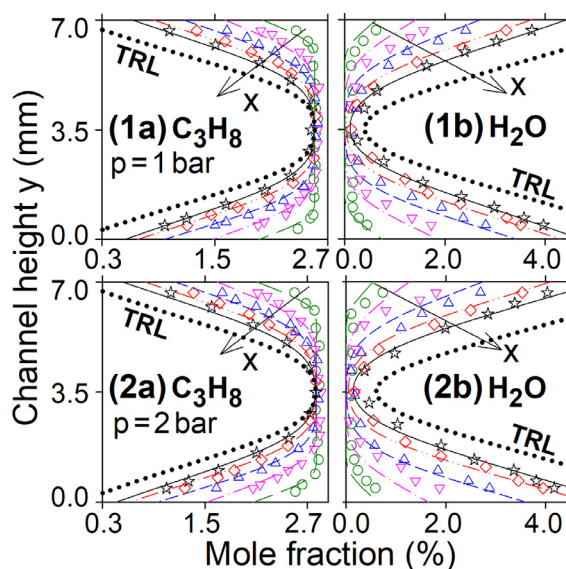
Fig. 2. Raman-measured (symbols) and simulated (lines) transverse profiles of C_3H_8 and H_2O mole fractions for Cases 1 and 2; $x = 8$ mm (circles, long-dashed lines), 36 mm (lower-triangles, dashed-dotted lines), 66 mm (upper-triangles, short-dashed lines), 96 mm (diamonds, dashed double-dotted lines), 126 mm (stars, solid lines). Dotted lines marked TRL are transport-limited simulations at $x = 126$ mm.

example, at 3, 4, 5 and 6 bar the computed C_3H_8 mole fractions were 14%, 17%, 19% and 23% lower than the measurements at the farthest downstream ($x = 126$ mm) and lowest transverse ($y \approx 0.6$ mm) positions (star symbols), as indicated by the horizontal thick gray bars in Figs. 3(3a-6a). The predicted C_3H_8 conversions in Cases 1–6 were less than 30% (see Fig. 5).

On the other hand, the differences between predicted and measured H_2O mole fractions in Figs. 2(1b-2b) and Figs. 3(3b-6b) were substantial for all pressures (see e.g. the horizontal thick bars in Figs. 3(3b-6b) pertaining to $x = 36$ and 66 mm). Such discrepancies may have been expected, as the employed mechanism [19] was fine-tuned for CPOX and not CTOX. This is clarified in Fig. S1 (supplementary material), providing computed species selectivities and mole fractions for Cases 1 and 6 for the C-containing and H-containing products. Therein, C_3H_8 was converted not only to CTOX but also to CPOX products (primarily CO and much less H_2), while a large amount of CH_4 was also produced. The Raman measurements have not shown production of such copious amounts of CO and CH_4 and this was additionally reported by gas-chromatography measurements in [18] during fuel-lean C_3H_8/air atmospheric-pressure combustion over Rh.

Our past studies of fuel-lean $CH_4/O_2/N_2$ oxidation over Pt [21], Rh [13] and PdO [25] have shown that a cardinal feature for the applicability of a high-pressure catalytic reaction mechanism is the correct prediction of the free-site coverage

reduction (and the corresponding oxygen coverage increase) with rising pressure. This behavior restrained the rate of increase of the catalytic reactivity with rising pressure. A one-step reaction for the CTOX of hydrocarbons, first-order with respect to the deficient fuel, has been shown suitable in past studies [13,21,25] and was also adopted for the C_3H_8 oxidation on Rh:

$$\dot{s}_{C3H8} = A \, (p/p_o)^{-n} \exp\left(-E_a \, / RT_w\right)[C_3H_8]_w, \quad (1)$$

with $\dot{s}_{C3H8}$ the catalytic molar reaction rate, A the pre-exponential, p_o a reference pressure, E_a the effective activation energy, T_w the wall temperature and $[C_3H_8]_w$ the concentration at the gas-wall interface. The positive exponent n in Eq. (1) restrained the increase of the reaction rate with rising pressure, since $\dot{s}_{C3H8} \sim p^{1-n}$ given that $[C_3H_8]_w \sim p$.

The kinetic parameter fitting was conducted using the surface perfectly stirred reactor (SPSR) package of Chemkin [33] along with 2-D channel simulations at 1-6 bar and temperatures 680-970 K. The global step in Eq. (1) with fitted parameters $E_a = 78$ kJ/mol, $A = 2.2 \times 10^5$ cm/s, $n = 0.86$ and $p_o = 1$ bar reproduced very well the Raman measurements (see comparisons in Fig. 6 for three selected cases). The deduced E_a was close to the value 74.7 kJ/mol reported in [18] at 1 bar. Note, in particular, the quite good agreement with the H_2O measurements in Figs. 6(1b, 4b, 6b), which attested the dominant CTOX behavior. The overall pressure dependence of the C_3H_8 reaction rate in Eq. (1) was $p^{0.14}$ ($= p^{1-n}$), which was much weaker compared to that on Pt ($p^{0.70}$ [26]). Hence, Pt was not only more
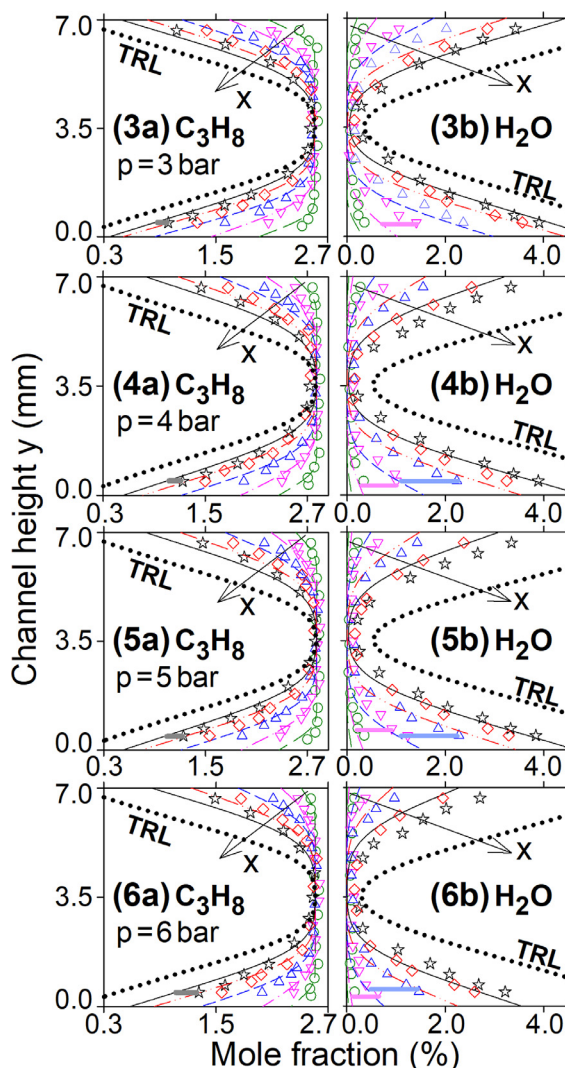
Fig. 3. Raman measured (symbols) and simulated (lines) transverse profiles of C_3H_8 and H_2O mole fractions for Cases 3-6. Colored horizontal bars denote differences between measurements and predictions. Notations as in Fig. 2.

active than Rh towards C_3H_8 CTOX at 1 bar [8] but also this trend accelerated at elevated pressures: the ratio of the 6-to-1 bar reactivities on Pt was 3.50 while this ratio on Rh was only 1.28. Qualitatively, the same trends were observed during CH_4 CTOX over Pt and Rh [13,21] albeit the differences were milder: the 6-to-1 bar reactivity ratio for CH_4 was 2.58 for Pt and 1.70 for Rh. Such intricate pressure dependencies were a result of the relative adsorption/desorption strengths of the fuel and oxygen on the particular catalyst.

X-ray Photoelectron Spectroscopy (XPS) was performed ex-situ on fresh samples and samples heated for 1 hr in an oven in atmospheric-pressure air. The spectra in Fig. S2 indicated that above 700 K, which were the catalyst surface temperatures of the present study (Fig. 4), the Rh_2O_3 (Rh^{+3}) phase was dominant. This actually aided the construction of the one-step kinetic model, as it negated potentially different activities on various Rh phases.

4.2. Gas-phase combustion

Comparisons between measured and predicted (using the one-step catalytic reaction of Eq. (1) and the San Diego gaseous mechanism [29]) 2-D OH distributions for Cases 7-11 are depicted in Fig. 7, while the wall temperatures and the C_3H_8 conversions are shown in Figs. 8 and 9 respectively. Gas-
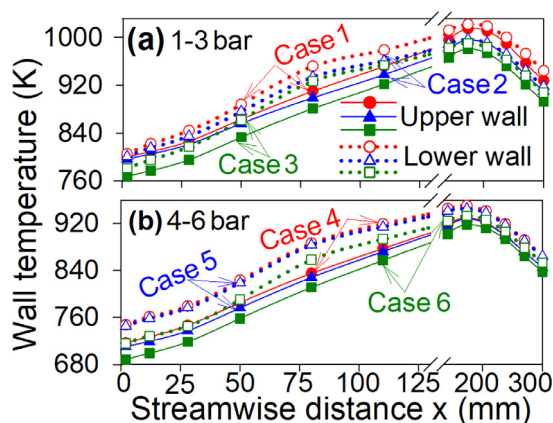
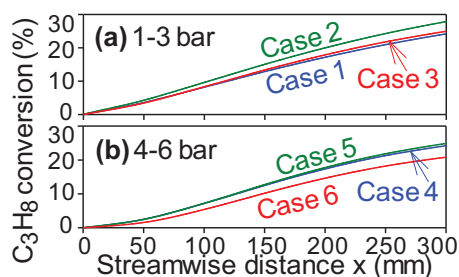Fig. 4. Measured upper-wall and lower-wall temperatures, Cases 1-6.

Fig. 5. Predicted C_3H_8 conversions, Cases 1–6.

phase combustion could not be ignited at pressures below 3 bar. Vertical arrows in Fig. 7 mark the onset of homogeneous ignition (x_{ig}), defined as the far-upstream axial location where OH attained 5% of its peak reactor value. The consistently shorter x_{ig} at higher pressures indicated promotion of homogeneous ignition with rising pressure. Following gaseous ignition, C_3H_8 was fully consumed (Fig. 9). The agreement between measured and predicted homogeneous ignition distances was good and was further improved with rising pressure. Characteristically, while the OH-PLIF at 3 bar yielded $x_{ig} = 251.0$ mm (Fig. 7(7a)) and the simulation $x_{ig} = 222.8$ mm (Fig. 7(7b)) with a resulting 11.2% discrepancy, the OH-PLIF and simulations at 4 bar (Case 9) had a x_{ig}-discrepancy of 8.4% and at 6 bar (Case 11) a x_{ig}-discrepancy of 2.5%. Radical adsorption/desorption reactions had a modest impact on the x_{ig}-position (typically up to ~5% [34]) and their absence in the global step of Eq. (1) could only account for a minor part of the
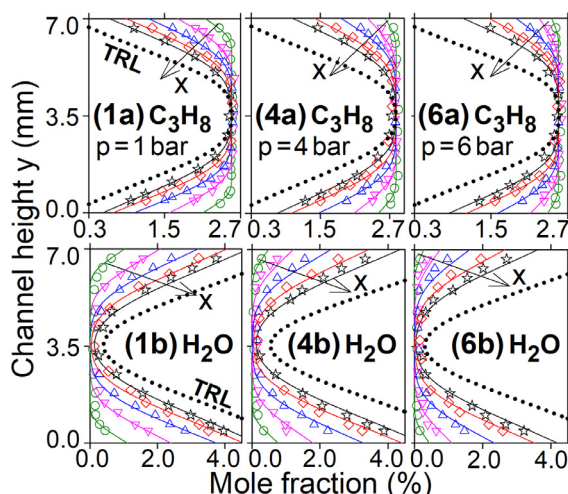

Fig. 6. Raman-measured (symbols) and simulated (lines, model of Eq. (1)) transverse profiles of C_3H_8 and H_2O mole fractions for Cases 1, 4 and 6. Symbol notations as in Fig. 2.
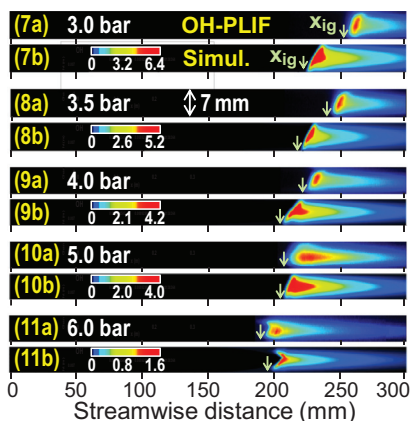
Fig. 7. Two-dimensional OH distributions for Cases 7-11 (a) –OH-PLIF and (b) simulations. Color-coded bars give the predicted OH (ppmv).

observed differences. As the largest differences occurred at lower pressures, wherein the simulations always underpredicted the measured x_{ig}, the employed hetero-/homogeneous reaction mechanisms provided a conservative simulation tool for assessing the gaseous ignition propensity in practical systems. Transverse profiles of temperature and major species mole fractions at the homogeneous ignition locations are given in Fig. S3 for Cases 7–11.

The hetero-/homogeneous chemistry coupling was finally investigated with SPSR [33] simulations. To decouple chemical from thermal effects, the SPSR surface temperature was maintained constant at 900 K, independent of the bulk gas temperature that could only be controlled by gaseous chemistry; nonetheless, both catalytic and gaseous reaction pathways participated to the species production/destruction. Residence times and surface-to-volume ratio were selected to ensure catalytic conversions of the deficient C_3H_8 reactant ∼40% of the total (catalytic and gaseous) consumption,
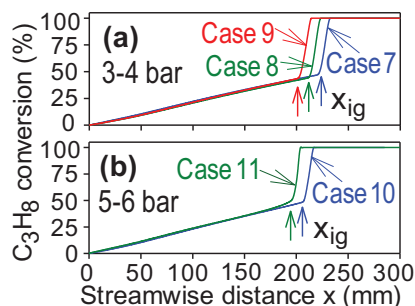

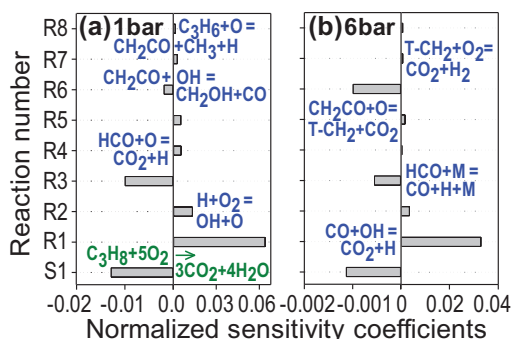Fig. 9. Predicted C_3H_8 conversions, Cases 7–11.

Fig. 10. Normalized sensitivity coefficients of temperature in an SPSR at 1 and 6 bar.

i.e. similar to those of Cases 7–11 (see Fig. 9). Normalized temperature sensitivity coefficients (SC) of the controlling reactions are shown in Fig. 10 for $p = 1$ and 6 bar, and for an inlet composition as in Case 11. The S1 in Fig. 10 denotes the catalytic reaction in Eq. (1) while R1-R8 are the most sensitive gaseous reactions.

The negative SC in S1 signified the suppression of homogeneous combustion due to the competing heterogeneous C_3H_8 consump-
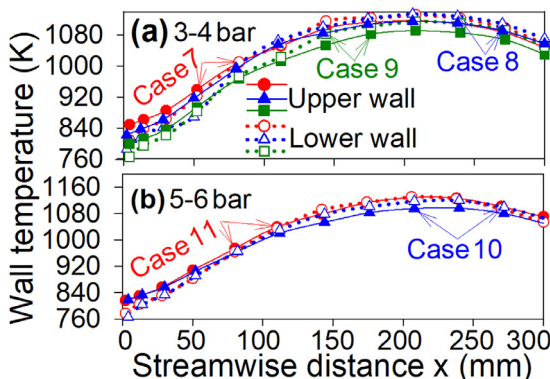

Fig. 8. Measured upper-wall and lower-wall temperatures, Cases 7-11.

tion. From the gaseous reactions, high pressures resulted in increased (negative) sensitivity especially for R6 ($CH_2CO + OH = CH_2OH + CO$) and decreased (negative) sensitivity for R3 ($HCO + M = CO + H + M$). Appropriate modifications of these reactions could improve the low-pressure predictions in Fig. 7.

5. Conclusions

The heterogeneous and homogeneous combustion of fuel-lean $C_3H_8/O_2/N_2$ mixtures over Rh was investigated at pressures $1 \le p \le 6$ bar and surface temperatures 680-1100 K. Measurements in a channel-flow catalytic reactor included Raman spectroscopy of major gas-phase species concentrations, planar laser induced fluorescence (PLIF) of the OH radical and thermocouple measurements of the surface temperatures, while 2-D simulations involved detailed hetero-/homogeneous chemistry. Raman-measured transverse species profiles in conjunction with numerical simulations led to the development of a suitable global reaction for the CTOX of propane. Literature catalytic mechanisms developed for CPOX were found inappropriate for the present CTOX (ultra-lean stoichiometries) conditions. It was shown that the propane CTOX reactivity over Rh had a weak pressure dependence $\sim p^{0.14}$, considerably lower than the $\sim p^{0.70}$ dependence of propane CTOX over Pt, thus suggesting care when selecting catalytic reactors for small-scale turbines and recuperative microreactors fueled with propane or LPG. XPS showed that, for the surface temperatures of this study, the Rh_2O_3 (Rh^{+3}) phase dominated, thus facilitating the development of the global catalytic step.

Simulations with the constructed global catalytic step and a detailed gas-phase mechanism yielded homogeneous ignition distances x_{ig} within 2.5% of the PLIF measurements at 6 bar. With decreasing pressure, the simulations led to progressively increasing underpredictions of x_{ig} (by as much as 11.2% at 3 bar), which was nonetheless a quite satisfactory performance for reactor design purposes. The key gaseous reactions affecting homogeneous combustion, identified via sensitivity analysis, were $CH_2CO+OH = CH_2OH+CO$ and $HCO+M = CO+H+M$.

Declaration of Competing Interest

None.

Acknowledgments

Supplementary materials

Supplementary material associated with this article can be found, in the online version, at doi:10.1016/j.proci.2020.06.029.

References

[1] R. Carroni, T. Griffin, *Catal. Today* 155 (2010) 2–12.
[2] S.B.M. Deshmukh, A. Krishnamoorthy, V.K. Bhojwani, *Heat Transf. Res.* 50 (2019) 1023–1041.
[3] S. Karagiannidis, K. Marketos, J. Mantzaras, R. Schaeren, K. Boulouchos, *Catal. Today* 155 (2010) 108–115.
[4] T.Y. Kim, C. Park, S. Oh, G. Cho, *Energy* 115 (2016) 386–396.
[5] J. Mantzaras, *Prog. Energy Combust. Sci.* 70 (2019) 169–211.
[6] S.S. Merchant, C.F. Goldsmith, A.G. Vandeputte, M.P. Burke, S.J. Klippenstein, W.H. Green, *Combust. Flame* 162 (2015) 3658–3673.
[7] M. Aryafar, F. Zaera, *Catal. Lett.* 48 (1997) 173–183.
[8] N. Kruse, A. Frennet, J.M. Bastin, Catalysis and Automotive Pollution Control IV, 116, Elsevier Science, 1998.
[9] G. Veser, M. Ziauddin, L.D. Schmidt, *Catal. Today* 47 (1999) 219–228.
[10] S.R. Deshmukh, D.G. Vlachos, *Combust. Flame* 149 (2007) 366–383.
[11] C.P. O'Brien, G.R. Jenness, H. Dong, D.G. Vlachos, I.C. Lee, *J. Catal.* 337 (2016) 122–132.
[12] T.F. Garetto, E. Rincon, C.R. Apesteguia, *Appl. Catal. B-Environ.* 48 (2004) 167–174.
[13] R. Sui, J. Mantzaras, R. Bombach, A. Denisov, *Proc. Combust. Inst.* 36 (2017) 4321–4328.
[14] X. Dong, K. Tsuneyama, T. Hibino, *Appl. Catal. B-Environ.* 106 (2011) 503–509.
[15] C.K. Ryu, M.W. Ryoo, I.S. Ryu, S.K. Kang, *Catal. Today* 47 (1999) 141–147.
[16] H. Jeong, G. Lee, B.S. Kim, J. Bae, J.W. Han, H. Lee, *J. Am. Chem. Soc.* 140 (2018) 9558–9565.
[17] K.A. Ledwa, L. Kepinski, M. Pawlyta, *Catal. Sci. Technol.* 9 (2019) 4633–4644.
[18] T.A. Wierzbicki, I.C. Lee, A.K. Gupta, *Appl. Energy* 130 (2014) 350–356.
[19] C. Karakaya, H. Karadeniz, L. Maier, O. Deutschmann, *ChemCatChem* 9 (2017) 685–695.
[20] M. Hartmann, L. Maier, H.D. Minh, O. Deutschmann, *Combust. Flame* 157 (2010) 1771–1782.
[21] M. Reinke, J. Mantzaras, R. Schaeren, R. Bombach, A. Inauen, S. Schenker, *Combust. Flame* 136 (2004) 217–240.
[22] M. Reinke, Mantzaras, R. Bombach, S. Schenker, N. Tylli, K. Boulouchos, *Combust. Sci. Technol.* 179 (2007) 553–600.
[23] D. Ciuparu, M.R. Lyubovsky, E. Altman, L.D. Pfefferle, A. Datye, *Catal. Rev. Sci. Eng.* 44 (2002) 593–649.
[24] H. Yamamoto, H. Uchida, *Catal. Today* 45 (1998) 147–151.

[25] R. Sui, J. Mantzaras, E.T. Es-sebbar, R. Bombach, *Proc. Combust. Inst.* 37 (2019) 5465–5472.

[26] S. Karagiannidis, J. Mantzaras, R. Bombach, S. Schenker, K. Boulouchos, *Proc. Combust. Inst.* 32 (2009) 1947–1955.

[27] X. Zheng, J. Mantzaras, R. Bombach, *Proc. Combust. Inst.* 34 (2013) 2279–2287.

[28] R. Sui, J. Mantzaras, R. Bombach, *Combust. Flame* 202 (2019) 292–302.

[29] San Diego mechanism chemical reaction mechanism, 2016-12-14. https://web.eng.ucsd.edu/mae/groups/combustion/mechanism.html.

[30] M.E. Coltrin, R.J. Kee, F.M. Rupley, Surface Chemkin: A Fortran package for analyzing heterogeneous chemical kinetics at the solid surface-gas phase interface. Sandia National Laboratories, Report No. SAND90-8003C, 1996.

[31] R.J. Kee, F.M. Rupley, J.A. Miller, Chemkin II: A Fortran chemical kinetics package for the analysis of gas-phase chemical kinetics. Sandia National Laboratories, Report No. SAND89-8009B, 1996.

[32] R.J. Kee, G. Dixon-Lewis, J. Warnatz, M.E. Coltrin, J.A. Miller, A Fortran computer code package for the evaluation of gas-phase multicomponent transport properties. Sandia National Laboratories, Report No. SAND86-8246, 1996.

[33] H.K. Moffat, R.J. Kee, J.F. Grcar, J.A. Miller, Surface PSR: A Fortran program for modeling well-stirred reactors with gas and surface reactions. Report No. SAND91-8001, Sandia National Laboratories, 1993.

[34] M. Reinke, J. Mantzaras, R. Schaeren, R. Bombach, W. Kreutner, A. Inauen, *Proc. Combust. Inst.* 29 (2002) 1021–1029.